Engraved split-ring resonators as potential microwave sensors for olive oil quality control

Zacharias Viskadourakis[1,], Anna Theodosi[1,2], Klytaimnistra Katsara[1,3], Maria Sevastaki[1,4], George Fanourakis[5], Odysseas Tsilipakos[6], Vassilis M. Papadakis[7,1] and George Kenanakis[1,*]*

[1] Institute of Electronic Structure and Laser (IESL), Foundation for Research and Technology – Hellas (FORTH), N. Plastira100, Vassilika Vouton, Heraklion GR-70013, Greece

[2] Department of Materials Science and Technology, University of Crete, Heraklion 70013, Greece

[3] Department of Agriculture, Hellenic Mediterranean University, Estavromenos, GR-71410 Heraklion, Greece

[4] Department of Chemistry, University of Crete,710 03 Heraklion, Crete, Greece

[5] Department of Electronics and Nanoengineering, School of Electrical Engineering, Aalto University, 02150 Espoo, Finland

[6] Theoretical and Physical Chemistry Institute, National Hellenic Research Foundation, GR-11635 Athens, Greece

[7] Department of Industrial Design and Production Engineering, University of West Attica, 12244 Athens, Greece

*Corresponding author: zach@iesl.forth.gr (Z.V.), gkenanak@iesl.forth.gr (G.K.)

KEYWORD: Split–Ring–Resonator, complementary metasurface, CNC engraving, oil sensor, olive oil quality sensor

ABSTRACT

In the current study, microwave complementary split ring resonators are explored, regarding their sensing capability against olive oil adulteration. In particular, millimeter-scale complementary split ring resonators were developed, employing the Computer Numerical Control method, in combination with a home-built mechanical engraver. Their electromagnetic behavior was comprehensively studied, both experimentally and theoretically, in the frequency range 1-9 GHz. Furthermore, their electromagnetic response was investigated in the presence of different types of edible oils, such as virgin olive oil, corn and soyabean oil. Both experimental results and theoretical simulations clearly reveal the distinct response of the fabricated complementary resonators, to the different oil types. Even more, they exhibit a significant response in oil mixtures, enabling the detection of possible adulteration in olive oil. Consequently, it becomes evident that mechanically – engraved microwave complementary split ring resonators can be efficiently realized as potential sensors for olive oil quality control.

1. INTRODUCTION

Olive oil is an edible oil, which is produced by squeezing the olive fruit. In general, olive oil can be classified into four grades, namely extra virgin (EVOO), virgin (VOO), lampant (LOO) and pomace oil (POO), considering the production method followed, its acidity and organoleptic quality and fruity. Regardless its grade, olive oil is highly beneficial on human health, due to its high content of oleic acid and polyphenols.[1,2] Olive oil exhibits antioxidant, anti-inflammatory, antimicrobial, and antitumor properties. [3–5] Moreover, consumption of olive oil has been associated with decreasing of the LDL-cholesterol, and thus suppressing of cardiovascular diseases, [6] as well as with enhanced sustainability against some kinds of cancer.[7,8] Thus olive oil is realized as a natural product with substantial nutrition value, valuable for human quality of life.

In addition, olive oil industry is a major income source, especially for Mediterranean countries, where olive trees are systematically cultivated. It is noteworthy that more than 75% of the total olive oil production comes from three countries, Spain, Italy and Greece, while the first seven producing countries in the global olive oil list are located around the Mediterranean Sea.[9] Moreover, the annual global olive oil consumption is approximately 2.5 – 3 megatones,[10] which corresponds to a total value of ~$10 – 15 billion. Therefore, olive oil market is a trade market, full of challenges and unfair competition. In order to reduce costs and increase the profit, olive oil processing and standardization companies use to mix EVOO with lower grade olive oils, as well as with other types of edible oils, such as corn oil, sunflower oil, coconut oil, soya bean oil, etc.[11–13] Hence, methods and procedures regarding the classification of olive oil, as well as the olive oil quality control against oil adulteration is highly required.

Currently, there are many processes relating to the quality control of olive oil; Apart from conventional physico-chemical analyses[14], these procedures include the use of various spectroscopic methods, such as Fourier Transformed Infrared Spectroscopy (FT – IR),[15] Ultraviolet – Visual spectroscopy (UV – Vis),[16] Fluorescence,[17] Raman spectroscopy,[18] Gas Chromatography – Mass spectroscopy[19], to name but a few. With the use of these optical techniques, detailed quality control can be achieved, such as a gentle classification of edible oils,[18] olive oil adulteration,[20] oil contamination and differentiation among oil types,[21] as well as olive oil grades.[22] Even more, combinations of the above–mentioned spectroscopic methods,[14,20] leads to higher resolutions, greater sensitivities and thus in more precise oil quality control. Therefore, the use of spectroscopic methods and techniques, can be considered as state-of-the-art procedures for olive oil quality control. However, all the above methods are laboratory oriented. Furthermore, highly experienced and well-trained personnel is required, in order to perform such spectroscopic experiments. In addition, spectroscopic instruments are quite complicated to their use, and the corresponding analysis of the obtained spectra is time consuming.

To avoid such obstacles, other kinds of oil quality sensors have been proposed, which are based on the application of artificial intelligence and machine learning in the acquisition and appropriate analysis of spectra.[23–28] In principle, a portable spectrometer is used in order to record multiple spectra, from several oil samples. Then, the collected spectra are subjected to analytic algorithms, leading to the determination of specific quantities, associated with oil quality. Such sensors are user-friendly, relatively cheap, while results are extracted rapidly. However, compared to the state-of-the-art methods, they do not demonstrate high resolution, while the use of analytical models and machine learning algorithms can introduce systematic errors and reduce the overall performance of sensors. Furthermore, multiple samples must be measured, each one for several times.

In this context, the development of an oil quality sensor, which will be portable, cheap, with quick response, user-friendly, accurate, with high sensitivity, without using algorithms, and complicated analytical models, is highly desirable. Taking all the above into account, metasurfaces may be proposed for such an application; Metasurfaces are defined as man-made, surfaces which exhibit substantial electromagnetic properties, that cannot be found in natural materials, such as perfect absorption, negative or large positive refractive index, magnetism at high frequencies, etc.[29,30] The basic component of a metasurface is called meta–atom, which is of specific shape and dimensions. The appropriate arrangement of similar meta–atoms in the space is tightly correlated to the electromagnetic response of the metasurface. Considering this, metasurfaces can be potentially used in numerous applications, such as antennas, splitters, modulators, shields, energy harvesters and sensors[30–34].

Split-Ring Resonators (SRRs) are a category of meta-atoms, which consist of a metallic loop with a gap (typical example of an SRR, with rectangular shape, is shown in Figures 1a and 1b) . Such meta-atom structures could exhibit sharp absorption at a certain frequency (resonance), depending on their dimensions.[35,36] For instance, millimeter – scale SRRs would show resonance frequencies in the microwave regime (approximately 1 – 100 GHz). Therefore millimeter – scale SRRs can be potentially used for applications in the microwave regime. In order to understand the basic electromagnetic behavior of an SRR, each one of them can be originally represented by an RLC electronic circuit, consisting of a resistor *R*, a capacitor *C* and an inductor *L*, connected in series. Basic electronic analysis shows that, an RLC circuit the resonates at a frequency, determined through the relation $f_{res} \propto 1/2\pi\sqrt{LC}$. Apparently, R and L are affected by the metallic stripe dimensions, while *C*, is related to the gap dimensions. By including a dielectric material ($\varepsilon' > 1$) into the gap, the overall capacitance of the metasurface increases, and the corresponding resonance frequency moves towards lower values. In such way the sensing capability of the SRR is enabled. There are numerous studies regarding the sensing properties of SRRs, against solid materials, liquids and gases.[37–41] More interestingly, there are reports, in which complementary SRRs (CSRRs) are realized as sensors, as well. [42–44] Complementary SRRs behave similarly to the SRRs, albeit they are the "negative counterpart" of them. The analogy in the response between SRRs and CSRRs is described by the Babinet principle.[45] Regarding oil quality sensing, several metasurface structures have been proposed, exhibiting good sensing capabilities.[46–50] Nonetheless, none of them are complementary. Consequently, CSRRs could be investigated as an alternative option for oil quality control.

Considering the above discussion, it would be interesting to investigate the potential use of CSRRs as microwave oil quality sensors. In this context we developed millimeter-scale CSRRs using the so-called Computer Numerical Control (CNC) method. Conventionally, CSRRs are fabricated employing the well-known Printed Circuit Board (PCB) technique. In general PCB technology is a well–established, factory–oriented technology, which is used to massively produce electronic circuits and components.[51,52] Although, PCB method is a rather complex procedure, including several steps of fabrication. [53,54] Even more, some of those steps require the use of chemicals, therefore such a technology cannot be considered as environmentally friendly. In addition, expensive and complicated infrastructure is needed, as well as highly–trained, experienced personnel is required to use such infrastructure. Alternatively CSRRs have been successfully developed, using more versatile routes, such as Fused Filament Fabrication (FFF).[55] This is a three-dimensional printing technique, using a polymer composite as starting material. In principle, the raw material is melted and extruded through a nozzle. The nozzle can be moved in all three x, y, and z axes. Thus, by appropriately manipulating the movement of the nozzle, the desired three – dimensional object can be formed, in a layer – by – layer process. Such a method is simpler, cheaper, user-friendly, as well as laboratory-oriented, comparing to the PCB method. Main drawback of the method is that almost all raw materials, that are commercially available, exhibit insulating properties, which is not desirable in SRR loops.

On the other hand, the fabrication of metasurfaces employing the so-called Computer Numerical Control (CNC) method, has been recently reported.[56] CNC milling is a subtractive fabrication process that uses rotating cutting tools to remove material from a starting stock piece, commonly referred as the workpiece. The CNC milling system typically consists of a worktable for positioning the workpiece, a cutting tool (most commonly an endmill), and an overhead spindle for securing and rotating the cutting tool. In general, the worktable can be moved in both x and y axes while the spindle with the cutting tool can be moved along the z axis. The spindle rotates the catting tool attached, at several hundreds of rpms. Thus, by the combined movement of both the worktable and the spindle, the cutting tool digs the workpiece at specific areas, so as the desired object is formatted. Usually, CNC is employed in manufacturing metal, plastic and wooden parts, with various cutting tools, such as lathes, mills, drills, etc. CNC method exhibits similar advantages with the FFF technique, previously discussed. Furthermore, it helps to automate the fabrication process, thus improving repeatability and precision, reducing human error, and adding advanced capabilities (e.g., the direct conversion of CAD models to finished parts).[57] Moreover, CNC process does not involve the use of chemicals, which are demanded in other manufacturing processes, making it particularly advantageous for printed circuit boards.[58,59] Furthermore, CNC method is dedicated for large-scale production, decreasing the production time and cost, while increasing the productive capability.

In the current study, the CNC method is combined with a mechanical engraver, so as CSRRs are successfully printed/engraved onto metallized surfaces. In such engraved metasurfaces, the material under test can be inserted into the engraved area, increasing the sensitivity of the metasurface, which is an advantage, in comparison to conventional SRRs (where the material under test must be inserted into the gap). Several CSRRs were fabricated, with various dimensions. The fabricated CSRRs were characterized concerning their electromagnetic performance and all of them exhibit distinct resonant behavior at certain frequencies, depending on their size. Moreover, their sensing capability was examined against various types of edible oil, such as virgin olive oil, corn oil and soya bean oil. It was found that the studied CSRRs show considerable sensing efficiency among different oil types. Even more, the CSRRs were tested against mixtures containing virgin olive and soya bean oils. It was shown that the investigated CSRRs reveal a distinct response to oil mixtures with varying olive-to-soya bean oil ratio, indicating their enhanced sensing capacity to adulteration of olive oil. Furthermore, the above-described experimental results were compared to the corresponding spectroscopic results, revealing a solid consistency. Independently, theoretical simulations were performed, and the extracted results come in good agreement with the experiments. Consequently, the engraved CSRRs are evidently promising candidates for applications in oil quality control.

2. METHODS

2.1 Metasurface Fabrication

The so-called rectangular CSRR design was chosen for the purpose of the current study, as it has been studied for several sensing applications in the past.[55,56]. Mechanical engraving method was used, in order to fabricate such metasurfaces (MSs), using a home-built CNC router. The fabrication sequence is the following: appropriate MS drawings were made, using the open-source drawing software EASEL (Inventables Inc., Chicago, USA). The same software was also used to transform each drawing to an appropriate G-code file, that can be read by the CNC router. At the same time, the software controls the movements of both the CNC router spindle and workbed. At the spindle, a thin metallic carpenter bit (diameter: Ø 0.5 mm) is attached. A typical plain FR-4 surface, covered by a 35 μm-thick film of pure Cu, is placed on the CNC bed. After appropriately calibration, the engraving procedure occurs. The CNC spindle with the bid starts rotating and ploughs the FR-4 surface removing parts of its Cu film, from specific regions, so as the final complementary CSRR is developed (i.e. Figure 1a). In all cases the depth of the engraved CSRRs was kept at 0.2mm.

2.2. Metasurface electromagnetic characterization

All fabricated CSRRs were studied regarding their electromagnetic response through transmission experiments, in the microwave regime. Particularly, the metasurfaces were measured, using a combination of a P9372A Vector Network Analyzer (VNA) (Keysight, California, USA, frequency range 300KHz – 9 GHz) and WR284 (2.4 – 4.8 GHz), WR187 (3.5 – 7 GHz) and WR137 (5 – 10 GHz) waveguides (Figure 1c), so that a frequency range 2 – 9 GHz is covered . Details, regarding the set-up and the measurement procedure were previously described.[55,56,60] Two different configurations were investigated, i.e., the CSRR is oriented so that the electric field component parallel (TE orientation – drawing in Figure 2a) and perpendicular to the gap (TM orientation – drawing in Figure 2c).

2.3. Metasurface sensing properties measurements

In order to study the sensing properties of the CSRRs, with respect to different types of edible oil, (i.e., virgin olive oil (VOO), soya bean oil (SO) and corn oil (CO)), microwave transmission experiments were conducted, using the experimental set–up, shown in Figure 1c. Traces of oil (~

2-5 mm^3, depending on the CSRR size) are included into the engraved area of the metasurface, and the corresponding transmission spectrum is recorded, each time. Transmission spectra for empty CSRRs are also recorded and considered as reference spectra.

Furthermore, the sensing properties of the CSRRs were studied, against oil mixtures. In particular, VOO was mixed with SO, in several volume ratios, so that various VOO/SO mixtures were made. After that, a small amount of each mixture was inserted into the engraved area of the CSRR and microwave transmission spectra were recorded, as previously described. In this set of experiments the VOO transmission spectrum is considered as reference spectrum.

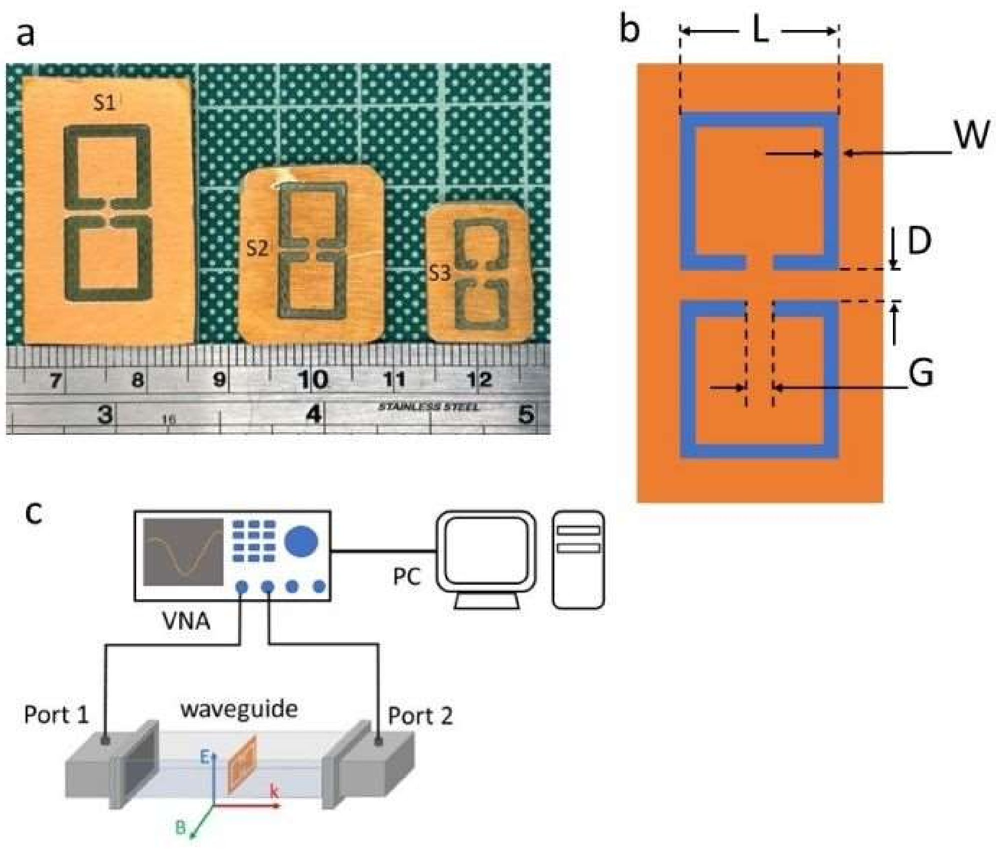

Figure 1. a. Picture of CSRRs used in the current study **b.** CSRR drawing, including critical dimensions **c.** Experimental set–up for electromagnetic characterization

2.4. Edible oil spectroscopic characterization

Before being used for the purposes of the current study, all types of oil, used hereby (purchased from the local market), such as VOO, CO and SO, were thoroughly characterized, employing various spectroscopic techniques. In particular, all three oils have been characterized through FT–IR, Raman, and UV–Vis spectroscopy. In particular, FT–IR experiments were carried out using a Bruker Vertex 70v FT–IR vacuum spectrometer in a spectral range of 3500 – 500 cm^{-1}, using a broad band KBr beamsplitter and a room temperature broad band triglycine sulfate (DTGS) detector; corresponding details can be found in previous work.[61] The obtained spectra (supplementary Figure S1a) are found to be similar to others previously reported.[62,63] On the other hand, Raman experiments were conducted at room temperature using LabRAM HR Evolution Confocal Raman Microscope (LabRAM HR; Horiba France SAS, Lille, France); experimental details are described in the literature.[56] Processing and analysis of the acquired raw Raman spectra were achieved through the instrument's original software (LabSpec, version LS6; Horriba, Lille, France). Initially, smoothing under a Gaussian filter with a kernel of five points (denoise at 5) was used, where cosmic rays were removed and the background was removed using a baseline correction at the sixth-order polynomial function. Corresponding Raman spectra (supplementary Figure S2a) show patterns consistent with others previously reported. [18,20,64,65] Finally, UV-Vis absorption spectra were collected, using K-MAC SV2100 spectrometer, in the wavelength range 300-900 nm; experimental details can be found elsewhere.[66] Recorded spectra (supplementary Figure S3a) demonstrate that only VOO shows distinct peaks within the measured range. Neither SO, or CO shows any spectroscopic feature in this range. All findings are consistent to previous reports. [67,68]

In addition, the dielectric permittivity of all oils was measured employing the standard coaxial probe method. An open-ended coaxial probe (N1501A dielectric probe kit, Keysight Technologies, CA, USA) was connected to the VNA (P9372A Streamline Vector Network Analyzer, Keysight, California, USA). The probe was immersed directly in the oil bath and the dielectric permittivity values (real and imaginary part) were automatically calculated through the VNA software (N1500A Materials Measurement Software Suite, Keysight, California, USA), in the frequency regime 1-9 GHz. Dielectric permittivity curves are presented in supplementary Figure S4.

2.5 Theoretical Simulations

Experimental results were further corroborated with theoretical simulations. The full–wave simulations with a continuous wave (CW) excitation were performed using the frequency domain solver of the commercial software CST Studio Suite. Two split ring resonators were engraved on a rectangular copper-coated FR–4 substrate and then the whole structure was inserted in the center of the waveguide. The copper layer was modelled via the electric conductivity of $5x10^7$ S/m, while the relative electric permittivity of the FR–4 substrate was considered to be 4–0.04i (loss tangent of 0.01). The waveguide walls were modeled as boundary conditions of Perfect Electric Conductor (PEC). This type of boundary condition sets the tangential component of the electric field to zero. The TE_{10} mode of the waveguide was used to excite the structure and the S–parameters were calculated by using the built-in rectangular waveguide ports. The adaptive mesh refinement option was selected in order to refine the mesh until achieving convergence for the calculated S–parameters. To introduce the different types of oils and mixtures within the engraved volume of the SRRs, we define additional geometric domains occupying the corresponding volumes in each case. The electromagnetic properties of each type of oil and mixture were described by the measured dispersive complex electric permittivity and inserted in the software via the dispersion material properties tab. Note that the mechanical properties of the liquids are not relevant to our electromagnetic simulations.

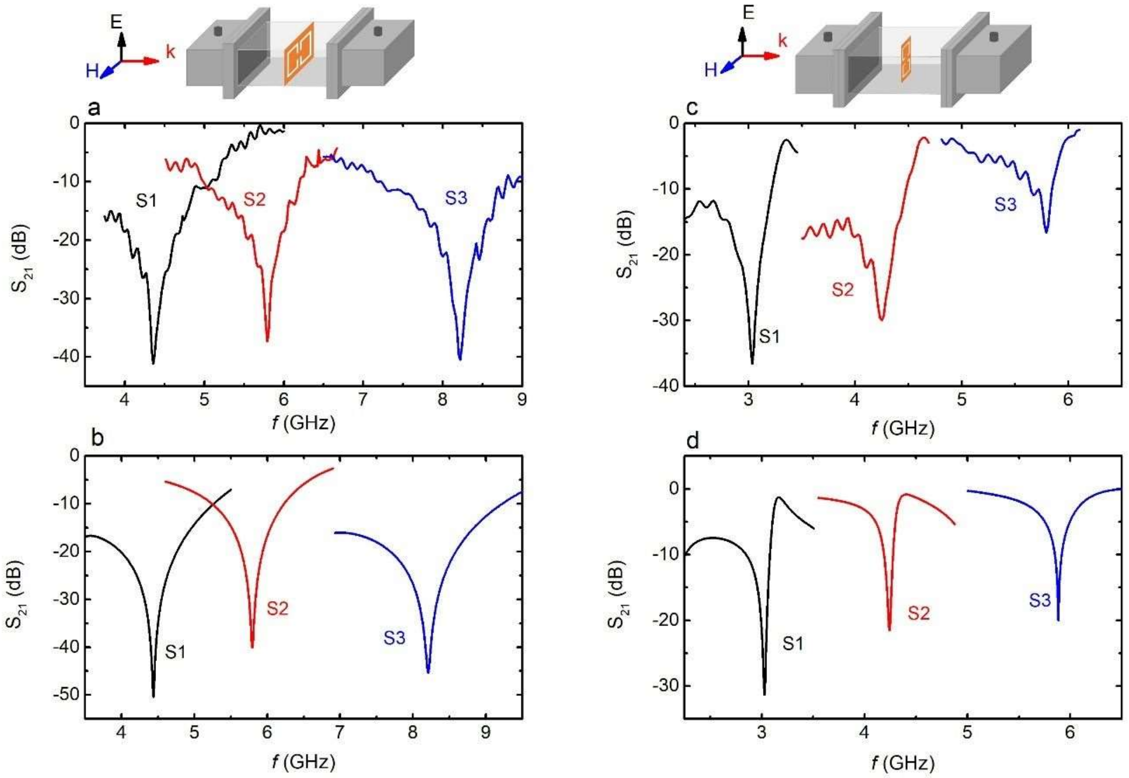

Figure 2. a. Transmission (S_{21} vs. f) spectra obtained for all CSRRs, in the TE orientation. The drawing above the panel a, shows the orientation of the CSRR into the waveguide. **b.** Corresponding theoretically simulated S_{21} vs. f, spectra, for the TE orientation **c.** S_{21} vs. f, obtained for all CSRRs, in the TM orientation, as shown in the drawing, above the panel **d.** Corresponding S_{21} vs. f spectra, as calculated from theoretical simulations.

3. RESULTS AND DISCUSSION

Figure 1a shows a typical picture of the studied CSRRs. Corresponding measured dimensions (Figure 1b) are shown in Table I. At first glance, larger samples, such as S1 and S2 are well-shaped, with opposite resonators perfectly aligned to each other. As the CSRR size is reduced, the engraved MSs show light deformations regarding their shape (i.e. Sample S3). On the other hand, the resonators are kept aligned to each other. In addition, the length L of the meta-atom varies from ~10 mm down to 6.5 mm. Such a variation will have an impact to their electromagnetic response, as shown later. Moreover, gap size G is almost similar for all metasurfaces. On the contrary, the line width W, varies with CSRR size decrement. Moreover, the distance D between the opposite split ring resonators, is different among samples. As it will be shown later, distinct electromagnetic response is observed for all metasurfaces, regardless the variations in width W and distance between resonators D.

CSRR	L (mm)	W(mm)	G (mm)	D (mm)	V (mm^3)
S1	10.3 ± 0.1	1.5 ± 0.1	1.1 ± 0.1	0.8 ± 0.05	10.2
S2	7.9 ± 0.1	1.3 ± 0.1	1.3 ± 0.1	0.5 ± 0.05	6.47
S3	6.5 ± 0.1	1.1 ± 0.1	1.3 ± 0.1	1.2 ± 0.1	4.47

Table I: Dimensions for all studied CSRRs. Corresponding volumes are calculated based on the given dimensions and considering the rectangular shape of the engraved area, as shown in Figure 1b.

Figure 2 shows the electromagnetic behaviour of all the metasurfaces. S_{21} vs. f spectra are presented for two different orientations, namely TE (drawing above Figure 2a) and TM (corresponding drawing above Figure 2c). In particular, sharp, well-defined minima are observed at specific frequency, for each engraved CSRR. Considering the negligible reflection observed for each MS (not shown here), the transmission minima are indicative of increased absorption of the incident electromagnetic wave. Therefore, all studied CSRRs resonate at certain frequencies. Resonance frequency increases with decreasing L, regardless the measured orientation (TE or TM). The above-described behaviour is theoretically corroborated with corresponding simulation results (Figures 2b and 2d). Moreover, such resonant behaviour has been previously shown for those CSRRs.[56] Consequently, all investigated CSRRs exhibit a considerable electromagnetic behaviour.

All CSRRs have been subjected to appropriate experiments, in order to confirm their electromagnetic response in the presence of VOO. In this context, we proceeded as follows; a tiny amount of VOO (~ 2 mm^3) was uniformly dispersed into the engraved area of each CSRR and the corresponding transmission spectrum was recorded. Experimental evidence is shown in Figure 3 (TE orientation). In particular, Figure 3a shows the transmission spectra for S1 sample, with VOO (red solid line) in comparison to the spectrum obtained for empty CSRR (black solid line). A slight (~18MHz), but distinguishable shift towards lower frequencies is observed. Similar behaviour is also observed for the S2 sample (Figure 3c), with a frequency shift of ~22MHz, while for the S3 sample a resonance shift of 98MHz is observed (figure 3e). Interestingly, all presented transmission curves are qualitatively consistent with corresponding results, extracted from appropriate theoretical simulations. In detail, simulations succeeded to reproduce the frequency shift, as well as its increment with decreasing CSRR size. Moreover, the calculated resonance shift for both S1 and S2 samples, is similar to the measured ones (Figures 3b and 3d, respectively). However, for S3 sample, the calculated frequency shift is larger than the measured (Figure 3f). In addition, theoretical results show that S_{21} minima become shallower, upon the introduction of VOO into the CSRR. Such a result is hardly seen in experimental findings for S1 and S2 samples, while it is exactly the opposite case with experimental results for S3 sample. Thus, there is a qualitative agreement between theoretical simulations and experimental evidence. Therefore, such a qualitative consistency seems adequate towards further exploration of the fabricated CSRRs, as potential oil quality sensors.

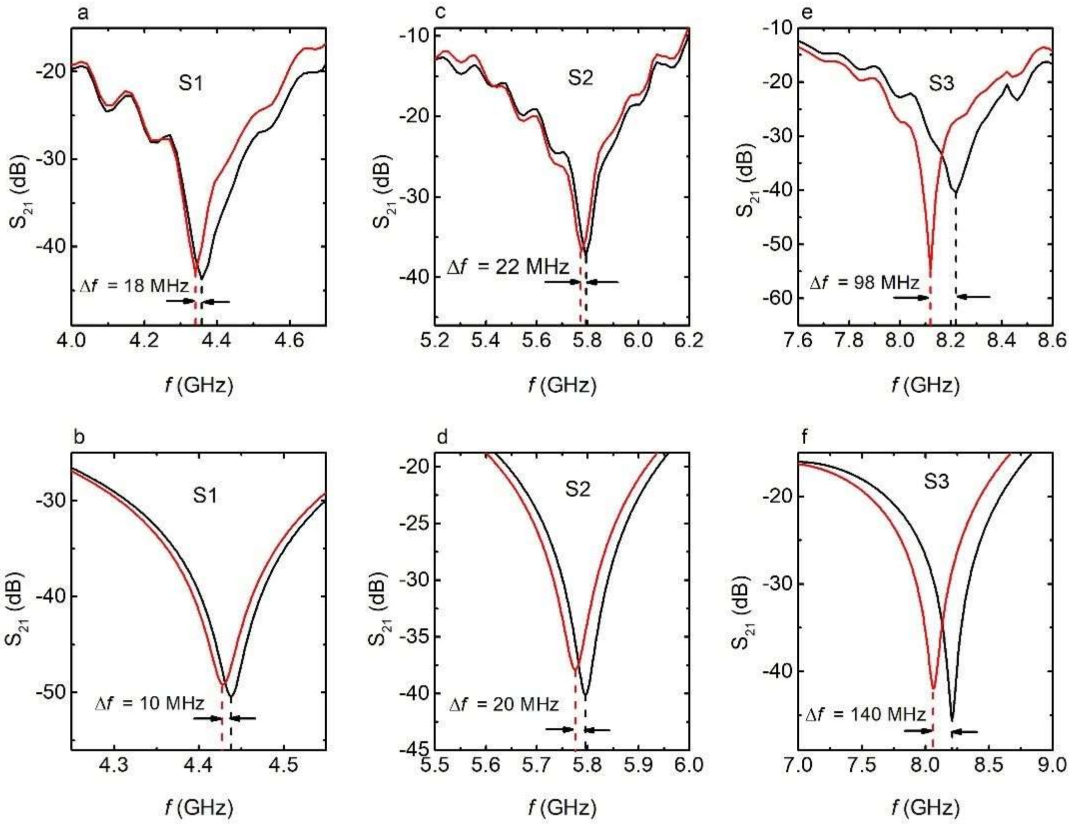

Figure 3. a. S_{21} vs. *f* spectra for S1 sample. Red line corresponds to the CSRR containing VOO oil into the engraved area, while black line corresponds to empty CSRR **b.** Corresponding theoretical simulation results for S1 sample **c.** S_{21} vs. *f* for S2 sample, with (red line) and without VOO (black line), into the engraved area **d.** Corresponding theoretical simulation results **e.** S_{21} vs. *f* for S3 sample, with (red line) and without VOO (black line), into the engraved area **f.** Corresponding theoretical simulation results.

In addition, the electromagnetic response of the CSRRs was investigated, with respect to VOO volume increments (i.e., typical behaviour for S2 sample in supplementary Figures S5a and S5c). It is observed that, as the VOO volume (included into the engraved area) increases, the resonant frequency moves towards lower values. Such a slight (a few MHz) shift of the resonance frequency can be is attributed to the low dielectric permittivity of the VOO. Furthermore, neither a considerable suppression of the dip was observed nor any elimination of the S_{21} minima was obtained, when filling the CSRR with maximum amount of oil. An agreement among experimental and theoretical results was also achieved (i.e, see supplementary Figures S5b and S5d).

The sensing capability of the CSRRs can be quantified through the quality factor *Q*, relative sensitivity *S*, and the Figure of Merit *FOM*. Quality factor *Q* is a dimensionless parameter, which designates the resonance curve sharpness, i.e, for sharp and slim resonance curves high quality factor values are obtained.[69,70] In addition, relative sensitivity *S%* is defined as the ratio of the resonance shift over the dielectric permittivity change.[71,72] In practice relative sensitivity shows the capability of the sensor to detect resonance shift, when oil is included into the engraved area of the CSRR. Finally Figure of Merit *FOM* is a parameter showing the overall performance of a sensing device.[71–73] Therefore, an efficient CSRR sensor would exhibit a very narrow and sharp resonance curve, when empty. However, upon inserting the tiniest possible amount of oil in to the engraved area, the resonance should abruptly move towards lower frequencies, while keeping its shape unaffected. All three parameters can be calculated, through the following relations:

$$Q = \frac{f_{res}}{FWHM} \quad (1)$$

$$S\,(\%) = 100 \times \frac{f_{emty} - f_{oil}}{f_{empty} \cdot (\varepsilon'_{oil} - 1)} \quad (2)$$

$$FoM = \frac{S}{FWHM} \quad (3)$$

where f_{res} is the resonance frequency, *FWHM* is the full width at half maximum of each electromagnetic minimum, f_{empty} is the resonance frequency of empty CSRR, f_{oil} is the resonance frequency of CSRR with oil included and ε'_{oil} is the dielectric permittivity of oil. Calculated *Q*, *S* and *FOM* values are presented in Table II, for all studied CSRRs.

Orientation	**Sample**	f_{empty} **(GHz)**	f_{oil} **(GHz)**	ε'_{oil}	***FWHM*** **(GHz)**	**Q**	**S(%)**	**FoM**
TE	**S1**	4.357	4.339	1.88	0.178	24.3	0.47	2.65
	S2	5.792	5.774	1.85	0.308	18.7	0.19	0.61
	S3	8.219	8.119	1.79	0.083	97.8	1.19	14.4
TM	**S1**	3.036	3.012	1.93	0.186	16.2	0.86	4.62
	S2	4.251	4.217	1.89	0.216	19.5	0.47	2.25
	S3	5.791	5.679	1.85	0.254	22.4	2.24	8.82

Table II: Calculated Quality factor Q, Sensitivity S and Figure of Merit, values for all CSRRs, in both measurement orientations

The observed *Q* and *FoM* values are greater, than those obtained for CSRR structures, proposed for water quality control,[56] indicating the enhanced performance of the CSRRs as oil sensors. The largest *FoM* value is achieved for the S3 sample (which is the smallest of all CSSRs) in both TE and TM orientations, evidently indicating its enhanced sensing behaviour, against oil.

It is worth noting that the *S* and *FoM* values, presented in Table II, are calculated, considering the transmission spectrum of the empty CSRR as reference spectrum. Consequently, upon the insertion of VOO into the engraved area of each metasurface, corresponding changes in the dielectric permittivity are large, leading to relatively low *S* and *FoM* in comparison to others reported so far, for split-ring resonator,s[46] dedicated for VOO sensing. Moreover, *FoM* values obtained here are also inferior to others reported for oil sensing MSs, of different shapes and types. [47,48] Nonetheless, the relatively high *Q* factors are comparable to those obtained for other split ring resonators[46] and other metasurfaces[47,48], which are proposed for oil sensing. Consequently, CSRRs arise as candidates with promising oil sensing capabilities.

To further investigate the oil sensing behaviour of the CSRRs, we proceed with experiments with other types of oil, such as SO and CO. Both of them exhibit higher dielectric permittivity than the VOO. Thus, it is prudent to explore the capability of the proposed CSRRs in distinguish among different types of oils. In this context, a fixed amount of oil (2 mm^3) is placed into the engraved area of the CSRR, and the corresponding transmission spectrum is recorded. Typical experimental results are presented in Figure 4, for S2 sample (corresponding experimental data for S1 and S3 samples are shown in supplementary Figures S6 and S7 respectively). It is noticeably seen that the CSRR resonates at different frequency, depending on the oil type (Figure 4a). Such an effect is observable in both TE and TM orientations (Figure 4a and 4c, respectively) and comes in qualitative agreement with corresponding theoretical simulation results (supplementary Figure S8). Interestingly, the resonance shift is directly related to the dielectric permittivity of oils, since the higher the dielectric permittivity the larger the resonance shift is achieved, as shown in Figure 4b and 4d, for both orientations. Moreover, the electromagnetic minimum shows a monotonic trend, regarding its depth, i.e., it decreases (in absolute values) with increasing dielectric permittivity, in the TE orientation (blue circles, Figure 4b), while it increases with increasing ε' in

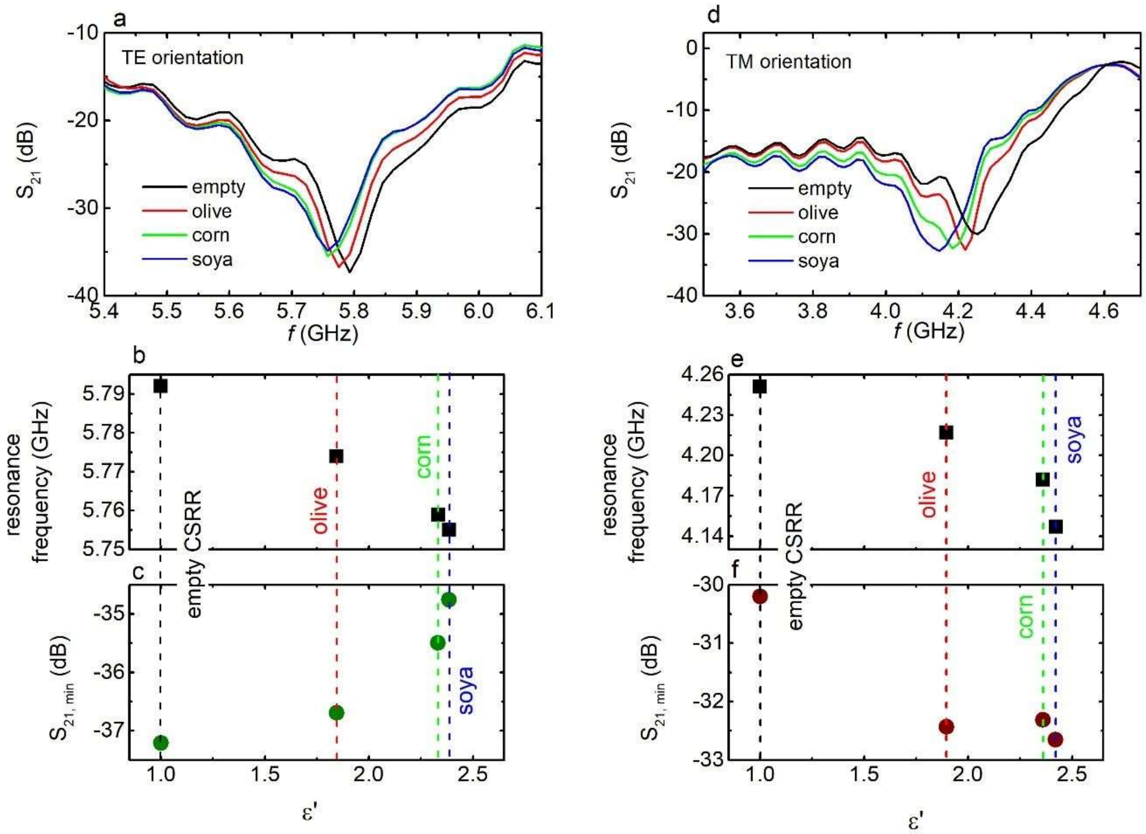

Figure 4. a. . S_{21} vs. *f*, with respect to various types of oil, for S2 sample (TE orientation) **b.** Resonance frequency and **c.** dip intensity, as a function of dielectric constant of oils. Both frequency and intensity values are extracted from panel a. Dash lines show the dielectric permittivity of each oil type. **d.** S_{21} vs. *f*, with respect to various types of oil, for S2 sample (TM orientation) **e.** Resonance frequency and **f.** dip intensity, as a function of dielectric constant of oil. Again, frequency and intensity values are extracted from panel c. Dash lines show the dielectric permittivity of each oil type.

the TM orientation (blue circles, Figure 4d). Hence, a discrete electromagnetic response is recorded for each type of oil, suggesting the capability of the studied CSRRs to operate as efficient oil sensors. Not only they effectively respond to the presence of small amounts of oil into the engraved area, but also, they differently behave to various types of oil. More interestingly, such a distinct electromagnetic response is demonstrated, with respect to oils with slightly different dielectric permittivity, such as CO and SO.

Here it is worth saying that the distinction among different types of oil is a challenging procedure. In most cases it is accomplished using spectroscopic techniques, described in the introduction. As previously discussed, corresponding experimental infrastructure for optical spectroscopy is complicated and expensive and it is used by dedicated personnel. Furthermore, analysis of the obtained spectra requires the use of sophisticated software, which, most of the times, is not available free–of–charge. In this context, the capability of the here–studied CSRRs to distinguish among various types of oil gives more credence to their potential use as oil sensors.

Since the investigated CSRRs exhibit such a sensitive response to the oil types, it would be of great interest to explore their electromagnetic behaviour in the presence of oil mixtures. In this point of view, we prepared mixtures consisting of VOO and SO, in several volume percentages (i.e., 10% v/v, 20% v/v, 50% v/v and 80% v/v). All mixtures have been characterized through spectroscopic methods, such as Raman, FT–IR, UV–Vis, and dielectric spectroscopy (supplementary Figure S1b, S2b, S3b and S9, respectively). In particular, characteristic Raman peaks for pure VOO, are observed at 1152 cm^{-} and 1515 cm^{-1} (supplementary Figure S2b). Both peaks are suppressed upon increasing the SO content, into the mixture, and they are both eliminated for pure SO. In addition, appropriate UV–Vis spectroscopy experiments show that VOO exhibits a characteristic peak at 670 nm, which is absent for all other oil types (supplementary Figure S3a). Such a peak is reduced, upon SO increment in oil mixtures, and it completely disappears for pure SO (supplementary Figure S3b). Considering the above–mentioned spectroscopic observations, a tiny amount (2

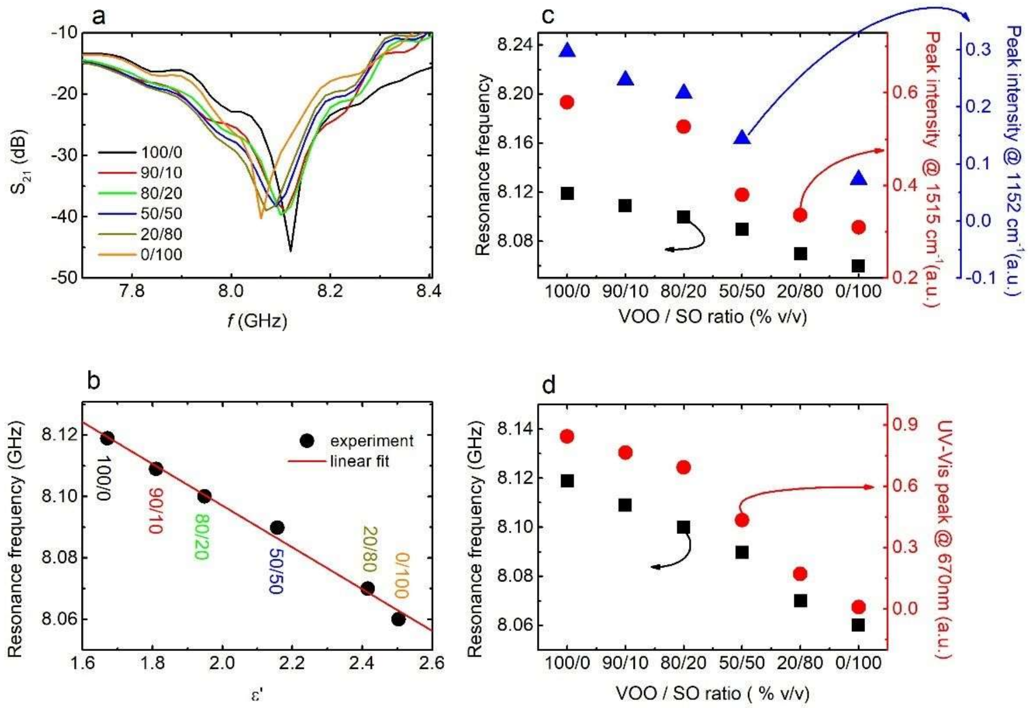

Figure 5. a. S_{21} vs. f, upon various VOO/SO mixtures, for S3 sample **b.** Resonance frequency evolution as a function of dielectric permittivity of oil mixtures. Each point corresponds to a specific VOO/SO oil mixture, as designated from matched labels. The colour of each label matches the colours of the curves, in panel a The red solid line corresponds to a linear fit **c.** Evolution of resonance frequency, with respect to the VOO/SO volume ratio (back rectangles), compared to the intensity evolution of Raman peaks at 1152 cm^{-1} (red circles) and 1515 cm^{-1}(blue triangles). Both Raman peaks are characteristic for VOO, and data presented hereby have been extracted from supplementary Figure S2a **d.** Resonance frequency, with respect to the VOO/SO volume ratio (back rectangles), compared to the intensity evolution of the UV–Vis 670 nm peak, characteristic for VOO. The UV–Vis data have been extracted from supplementary Figure S3b.

mm^3) of each oil mixture, was placed into the engraved area of the S3 CSRR and corresponding transmission spectra are recorded. Obtained patterns are presented in Figure 5. Moreover critical values are presented in Table III.

Oil mixture volume ratio (% v/v)	f_{res} (GHz)	ε'_{oil}	*FWHM* (GHz)	Raman peak 1152 cm^{-1} (a.u.)	Raman peak 1515 cm -1 (a.u.)	UV-Vis peak 670 nm (a.u.)
100/0	8.119	1.790	0.082	0.297	0.629	0.847
90/10	8.109	1.811	0.140	0.246	–	0.765
80/20	8.101	1.949	0.152	0.225	0.5276	0.693
50/50	8.089	2.157	0.186	0.152	0.379	0.440
20/80	8.072	2.416	0.180	–	0.337	0.170
0/100	8.063	2.504	0.111	0.071	0.311	0.011

Table III: Resonance frequency, dielectric permittivity and FWHM values, for several oil mixtures, measured in sample S3. Corresponding Raman and UV–Vis peak values, as extracted from Figures 5c and 5d. The resonance shift towards lower values, comes in consistency with the suppression of the spectroscopic peaks.

A slight, although well-defined shift, of the dip, towards lower frequencies is observed, with SO percentage increasing (Figure 5a). Considering the increment of the dielectric permittivity with increasing SO loading, the frequency shift is gradually enhanced with increasing *ε'* of the mixture (Figure 5b), in a fairly linear trend. A slope of -0.068 ±0.003 GHz / PU (PU: permittivity unit) can be extracted. Similar linear behaviour is also extracted from corresponding theoretical simulations (i.e. supplementary Figure S10b). The sensitivity of the CSRR, can be calculated by appropriately modifying relation (2), as follows:

$$S(\%) = 100 \times \frac{f_{mix} - f_{VOO}}{f_{VOO} \cdot \left(\varepsilon'_{mix} - e'_{VOO}\right)} = 100 \times \frac{\Delta f}{f_{VOO} \cdot \Delta\varepsilon'} = 0.83\%$$

where, $\frac{\Delta f}{\Delta\varepsilon'} = -0.068$. Moreover, considering an average FWHM ~ 0.140 GHz, as extracted from Table III, a *FoM* ~ 5.48 is obtained.

Both *S* and *FoM* values are still inferior than others reported so far, for several olive oil sensors.[47–50] However, the resonance frequency shift comes in perfect agreement with spectroscopic evidence. As previously discussed, Raman spectrum for VOO shows two distinct peaks at 1515 cm^{-1} and at 1152 cm^{-1} respectively, which are not presented in spectra of other oil types (supplementary Figure S2a). Both of them are gradually supressed as the SO percentage increases, in the oil mixture and, eventually, they are almost eliminated for pure SO (supplementary Figure S2b). The recorded frequency shift closely follows such a behaviour (Figure 5c), suggesting complete consistency. Even more, considering the UV–Vis spectra (supplementary Figure S3b), it is evidently shown that only VOO exhibits peaks, within the measured regime. For example, the peak at 670 nm, is progressively reduced with increasing SO inclusion loading (Figure 5d), until it vanishes for pure SO, directly tracking the gradual reduction of the resonance frequency. Therefore, regardless its low *FoM* the CSRR exhibits a rather effective performance, regarding the adulteration of the VOO with SO, which is concretely corroborated by both theoretical and spectroscopic evidence.

4. SUMMARY AND CONCLUSIONS

In summary, millimeter-scale CSRRs have been successfully developed, employing CNC method, in combination with a home-built mechanical engraver. Several samples were fabricated with varying dimensions concerning their length, line width, gap size etc. All metasurfaces are well-defined with straight lines. Their dimensions are quite similar to the dimensions of the initial drawings made, for the engraving purposes.

The produced CSRRs were thoroughly investigated, regarding their electromagnetic response, in the microwave regime. All of them display distinct dips in their transmission spectra, at certain frequencies, indicative of absorption of the incident wave. The resonance frequency is directly affected by the CSRR size, with the highest resonant frequencies to be exhibited by the smallest samples. The extracted experimental data are in agreement with corresponding theoretical simulation results. Furthermore, the electromagnetic behaviour of CSRRs is identical to that observed for conventional SRRs of similar dimensions.

By introducing traces of VOO into the engraved area of the CSRR, the resonance frequency moves to lower values. The resonance frequency shift becomes larger with decreasing the CSRR size. Moreover, this shift increases with increasing oil volume inserted into the engraved area. Both of those observations evidently reveal the sensing capability of the studied CSRRs, in the presence of VOO. In addition, the studied CSRRs were subjected in experiments with other edible oil types, namely CO and SO. All CSRRs exhibit distinct electromagnetic response, depending on the oil type, enabling the ability of the engraved metasurfaces to directly distinguish among different oil types. Even more, further electromagnetic response experiments with VOO/SO mixtures, in various ratios, are performed. Experimental results definitely show that the resonance frequency is reduced with increasing the SO inclusion into the oil mixture. Such experimental evidence comes in perfect agreement with corresponding spectroscopic results, obtained at the same time, as well as theoretical simulation results, and reveal the significant sensing capability in distinguishing among different oil mixtures.

In conclusion, both experimental and theoretical results, concretely suggest the capability of the engraved CSRRs to be potentially used as olive oil quality sensors.

Supporting Information.

Figure S1: FT – IR characterization of several edible oils; **Figure S2:** Raman characterization of several edible oils; Figure S3: UV – Vis characterization of several edible oils**;** Figure S4: Dielectric permittivity of edible oils; **Figure S5:** Electromagnetic Response of CSRRs with respect to the olive oil volume, under sense; **Figure S6:** Electromagnetic response of CSRRs with respect to the edible oil type, sample S1; **Figure S7:** Electromagnetic response of CSRRs with respect to the edible oil type, sample S3; **Figure S8:** Theoretical simulation results regarding the electromagnetic response of CSRRs with respect to the edible oil type; **Figure S9:** Dielectric characterization of VOO / SO mixtures; **Figure S10:** Theoretical simulation results regarding the electromagnetic response of CSRRs, for various VOO/SO mixtures

AUTHOR INFORMATION

Corresponding Author

zach@iesl.forth.gr (Z.V); gkenanak@iesl.forth.gr (G.K)

Author Contributions

The manuscript was written through contributions of all authors. All authors have given approval to the final version of the manuscript.

Notes

The authors declare no competing financial interest.

ACKNOWLEDGMENTS

K. K. acknowledges the Hellenic Foundation for Research and Innovation (HFRI) under the 4th Call for HFRI PhD Fellowships (Fellowship Number: 10660)

REFERENCES

(1) Tulipani, S.; Martinez Huelamo, M.; Rotches Ribalta, M.; Estruch, R.; Ferrer, E. E.; Andres-Lacueva, C.; Illan, M.; Lamuela-Raventós, R. M. Oil Matrix Effects on Plasma Exposure and Urinary Excretion of Phenolic Compounds from Tomato Sauces: Evidence from a Human Pilot Study. *Food Chem.* **2012**, *130* (3), 581–590. https://doi.org/https://doi.org/10.1016/j.foodchem.2011.07.078.

(2) Bendini, A.; Cerretani, L.; Carrasco-Pancorbo, A.; Gómez-Caravaca, A. M.; Segura-

Carretero, A.; Fernández-Gutiérrez, A.; Lercker, G. Phenolic Molecules in Virgin Olive Oils: A Survey of Their Sensory Properties, Health Effects, Antioxidant Activity and Analytical Methods. An Overview of the Last Decade Alessandra. *Molecules* **2007**, *12* (8), 1679–1719. https://doi.org/10.3390/12081679.

(3) Giovannini, C.; Masella, R. Role of Polyphenols in Cell Death Control. *Nutr. Neurosci.* **2012**, *15* (3), 134–149. https://doi.org/10.1179/1476830512Y.0000000006.

(4) Imran, M.; Nadeem, M.; Gilani, S. A.; Khan, S.; Sajid, M. W.; Amir, R. M. Antitumor Perspectives of Oleuropein and Its Metabolite Hydroxytyrosol: Recent Updates. *J. Food Sci.* **2018**, *83* (7), 1781–1791. https://doi.org/https://doi.org/10.1111/1750-3841.14198.

(5) Fei, P.; Ali, M. A.; Gong, S.; Sun, Q.; Bi, X.; Liu, S.; Guo, L. Antimicrobial Activity and Mechanism of Action of Olive Oil Polyphenols Extract against Cronobacter Sakazakii. *Food Control* **2018**, *94*, 289–294. https://doi.org/https://doi.org/10.1016/j.foodcont.2018.07.022.

(6) Estruch, R.; Martínez-González, M. Á.; Corella, D.; Salas-Salvadó, J.; Ruiz-Gutiérrez, V.; Covas, M. I.; Fiol, M.; Gómez-Gracia, E.; López-Sabater, M. C.; Vinyoles, E.; Arós, F.;

Conde, M.; Lahoz, C.; Lapetra, J.; Sáez, G.; Ros, E. Effects of a Mediterranean-Style Diet on Cardiovascular Risk Factors. *Ann. Intern. Med.* **2006**, *145* (1), 1–11. https://doi.org/10.7326/0003-4819-145-1-200607040-00004.

(7) Markellos, C.; Ourailidou, M.-E.; Gavriatopoulou, M.; Halvatsiotis, P.; Sergentanis, T. N.; Psaltopoulou, T. Olive Oil Intake and Cancer Risk: A Systematic Review and Meta-Analysis. *PLoS One* **2022**, *17* (1), e0261649. https://doi.org/10.1371/journal.pone.0261649.

(8) Emma, M. R.; Augello, G.; Di Stefano, V.; Azzolina, A.; Giannitrapani, L.; Montalto, G.; Cervello, M.; Cusimano, A. Potential Uses of Olive Oil Secoiridoids for the Prevention and Treatment of Cancer: A Narrative Review of Preclinical Studies. *Int. J. Mol. Sci.* **2021**, *22* (3), 1234. https://doi.org/10.3390/ijms22031234.

(9) *Olive Oil and Health*; Corrigan, J. D., Ed.; Nova Science Publishers.

(10) Sales, H.; Nunes, J.; Vaz Patto, M. C. Achievements and Challenges towards a Sustainable Conservation and Use of 'Galega Vulgar' Olea Europaea Variety. *Agronomy* **2020**, *10* (10), 1467. https://doi.org/10.3390/agronomy10101467.

(11) Jabeur, H.; Zribi, A.; Bouaziz, M. Extra-Virgin Olive Oil and Cheap Vegetable Oils:

Distinction and Detection of Adulteration as Determined by GC and Chemometrics. *Food Anal. Methods* **2016**, *9* (3), 712–723. https://doi.org/10.1007/s12161-015-0249-9.

(12) Luo, Y.; Gao, B.; Zhang, Y.; Yu, L. L. Detection of Olive Oil Adulteration with Vegetable Oils by Ultra-Performance Convergence Chromatography-Quadrupole Time-of-Flight Mass Spectrometry (UPC(2)-QTOF MS) Coupled with Multivariate Data Analysis Based on the Differences of Triacylglycerol Compo. *Food Sci. Nutr.* **2020**, *8* (7), 3759–3767. https://doi.org/10.1002/fsn3.1664.

(13) Aykas, D. P.; Karaman, A. D.; Keser, B.; Rodriguez-Saona, L. Non-Targeted Authentication Approach for Extra Virgin Olive Oil. *Foods* **2020**, *9* (2), 221. https://doi.org/10.3390/foods9020221.

(14) Gargouri, B.; Ben Hmida, R.; Koseoglu, O.; Bouaziz, M. Physico-Chemical Analysis of Virgin Olive Oils from Fresh and Fallen Fruits for Assessing the Quality and Shelf Life: Characterization by Chemometrics. *Eur. Food Res. Technol.* **2023**, *249* (10), 2705–2717. https://doi.org/10.1007/s00217-023-04308-8.

(15) Tarhan, İ.; Ismail, A. A.; Kara, H. Quantitative Determination of Free Fatty Acids in Extra

Virgin Olive Oils by Multivariate Methods and Fourier Transform Infrared Spectroscopy Considering Different Absorption Modes. *Int. J. Food Prop.* **2017**, *20* (sup1), S790–S797. https://doi.org/10.1080/10942912.2017.1312437.

(16) Gao, B.; Zhang, J.; Lu, W. Characterizing Variances of Adulterated Extra Virgin Olive Oils by UV-Vis Spectroscopy Combined with Analysis of Variance-Projected Difference Resolution (ANOVA-PDR) and Multivariate Classification. *Appl. Sci.* **2023**, *13* (7), 4360. https://doi.org/10.3390/app13074360.

(17) Martín-Tornero, E.; Fernández, A.; Durán-Merás, I.; Martín-Vertedor, D. Fluorescence Monitoring Oxidation of Extra Virgin Olive Oil Packed in Different Containers. *Molecules* **2022**, *27* (21), 7254. https://doi.org/10.3390/molecules27217254.

(18) Duraipandian, S.; Petersen, J. C.; Lassen, M. Authenticity and Concentration Analysis of Extra Virgin Olive Oil Using Spontaneous Raman Spectroscopy and Multivariate Data Analysis. *Appl. Sci.* **2019**, *9* (12), 2433. https://doi.org/10.3390/app9122433.

(19) Abdelrahman, M. H.; Hussain, R. O.; Shaheed, D. S.; AbuKhader, M.; Khan, S. A. Gas Chromatography-Mass Spectrometry Analysis and in Vitro Biological Studies on Fixed Oil

Isolated from the Waste Pits of Two Varieties of Olea Europaea L. *OCL* **2019**, *26* (28), 28.

(20) Philippidis, A.; Poulakis, E.; Papadaki, A.; Velegrakis, M. Comparative Study Using Raman and Visible Spectroscopy of Cretan Extra Virgin Olive Oil Adulteration with Sunflower Oil. *Anal. Lett.* **2017**, *50* (7), 1182–1195. https://doi.org/10.1080/00032719.2016.1208212.

(21) Kwofie, F.; Lavine, B. K.; Ottaway, J.; Booksh, K. Differentiation of Edible Oils by Type Using Raman Spectroscopy and Pattern Recognition Methods. *Appl. Spectrosc.* **2020**, *74* (6), 645–654. https://doi.org/10.1177/0003702819888220.

(22) Stefas, D.; Gyftokostas, N.; Kourelias, P.; Nanou, E.; Kokkinos, V.; Bouras, C.; Couris, S. Discrimination of Olive Oils Based on the Olive Cultivar Origin by Machine Learning Employing the Fusion of Emission and Absorption Spectroscopic Data. *Food Control* **2021**, *130*, 108318. https://doi.org/https://doi.org/10.1016/j.foodcont.2021.108318.

(23) Grossi, M.; Valli, E.; Bendini, A.; Gallina Toschi, T.; Riccò, B. A Portable Battery-Operated Sensor System for Simple and Rapid Assessment of Virgin Olive Oil Quality Grade. *Chemosensors* **2022**, *10* (3), 102. https://doi.org/10.3390/chemosensors10030102.

(24) Ordukaya, E.; Karlik, B. Quality Control of Olive Oils Using Machine Learning and Electronic Nose. *J. Food Qual.* **2017**, *2017*, 9272404. https://doi.org/10.1155/2017/9272404.

(25) Martínez Gila, D. M.; Gámez García, J.; Bellincontro, A.; Mencarelli, F.; Gómez Ortega, J. Fast Tool Based on Electronic Nose to Predict Olive Fruit Quality after Harvest. *Postharvest Biol. Technol.* **2020**, *160*, 111058. https://doi.org/https://doi.org/10.1016/j.postharvbio.2019.111058.

(26) Zarezadeh, M. R.; Aboonajmi, M.; Ghasemi-Varnamkhasti, M. The Effect of Data Fusion on Improving the Accuracy of Olive Oil Quality Measurement. *Food Chem. X* **2023**, *18*, 100622. https://doi.org/https://doi.org/10.1016/j.fochx.2023.100622.

(27) Venturini, F.; Sperti, M.; Michelucci, U.; Herzig, I.; Baumgartner, M.; Caballero, J. P.; Jimenez, A.; Deriu, M. A. Exploration of Spanish Olive Oil Quality with a Miniaturized Low-Cost Fluorescence Sensor and Machine Learning Techniques. *Foods* **2021**, *10* (5), 1010. https://doi.org/10.3390/foods10051010.

(28) Abu-Khalaf, N.; Hmidat, M. Visible/Near Infrared (VIS/NIR) Spectroscopy as an Optical

Sensor for Evaluating Olive Oil Quality. *Comput. Electron. Agric.* **2020**, *173*, 105445. https://doi.org/https://doi.org/10.1016/j.compag.2020.105445.

(29) Cui, T. J. Microwave Metamaterials. *Natl. Sci. Rev.* **2018**, *5* (2), 134–136. https://doi.org/10.1093/nsr/nwx133.

(30) Zografopoulos, D. C.; Tsilipakos, O. Recent Advances in Strongly Resonant and Gradient All-Dielectric Metasurfaces. *Mater. Adv.* **2023**, *4* (1), 11–34. https://doi.org/10.1039/D2MA00910B.

(31) Xie, L.; Gao, W.; Shu, J.; Ying, Y.; Kono, J. Extraordinary Sensitivity Enhancement by Metasurfaces in Terahertz Detection of Antibiotics. *Sci. Rep.* **2015**, *5* (1), 8671. https://doi.org/10.1038/srep08671.

(32) Ray, N. J.; Yoo, J.-H.; Nguyen, H. T.; Johnson, M. A.; Felgenbaum, E. Birefringent Glass-Engraved Tilted Pillar Metasurfaces for High Power Laser Applications. *Adv. Sci.* **2023**, *23* (10), 2301111. https://doi.org/https://doi.org/10.1002/advs.202301111.

(33) Xu, H.-X.; Tang, S.; Ma, S.; Luo, W.; Cai, T.; Sun, S.; He, Q.; Zhou, L. Tunable Microwave Metasurfaces for High-Performance Operations: Dispersion Compensation and Dynamical

Switch. *Sci. Rep.* **2016**, *6* (1), 38255. https://doi.org/10.1038/srep38255.

(34) Chiang, W.-F.; Silalahi, H. M.; Chiang, Y.-C.; Hsu, M.-C.; Zhang, Y.-S.; Liu, J.-H.; Yu, Y.; Lee, C.-R.; Huang, C.-Y. Continuously Tunable Intensity Modulators with Large Switching Contrasts Using Liquid Crystal Elastomer Films That Are Deposited with Terahertz Metamaterials. *Opt. Express* **2020**, *28* (19), 27676–27687. https://doi.org/10.1364/OE.399581.

(35) Gundogdu, T. F.; Gökkavas, M.; Güven, K.; Kafesaki, M.; Soukoulis, C. M.; Ozbay, E. Simulation and Micro-Fabrication of Optically Switchable Split Ring Resonators. *Photonics Nanostructures - Fundam. Appl.* **2007**, *5* (2), 106–112. https://doi.org/https://doi.org/10.1016/j.photonics.2007.07.001.

(36) Soukoulis, C. M.; Koschny, T.; Zhou, J.; Kafesaki, M.; Economou, E. N. Magnetic Response of Split Ring Resonators at Terahertz Frequencies. *Phys. status solidi* **2007**, *244* (4), 1181–1187. https://doi.org/https://doi.org/10.1002/pssb.200674503.

(37) Tabassum, S.; Nayemuzzaman, S. K.; Kala, M.; Kumar Mishra, A.; Mishra, S. K. Metasurfaces for Sensing Applications: Gas, Bio and Chemical. *Sensors* **2022**, *22* (18),

6896. https://doi.org/10.3390/s22186896.

(38) Buragohain, A.; Das, G. S.; Beria, Y.; Al-Gburi, A. J. A.; Kalita, P. P.; Doloi, T. Highly Sensitive Differential Hexagonal Split Ring Resonator Sensor for Material Characterization. *Sensors Actuators A Phys.* **2023**, *363*, 114704. https://doi.org/https://doi.org/10.1016/j.sna.2023.114704.

(39) Navaei, M.; Rezaei, P.; Kiani, S. Microwave Split Ring Resonator Sensor for Determination of the Fluids Permittivity With Measurement of Human Milk Samples. *Radio Sci.* **2022**, *57* (7), e2022RS007435. https://doi.org/https://doi.org/10.1029/2022RS007435.

(40) Alrayes, N.; Hussein, M. I. Metamaterial-Based Sensor Design Using Split Ring Resonator and Hilbert Fractal for Biomedical Application. *Sens. Bio-Sensing Res.* **2021**, *31*, 100395. https://doi.org/https://doi.org/10.1016/j.sbsr.2020.100395.

(41) Alibakhshikenari, M.; Virdee, B. S.; Elwi, T. A.; Lubangakene, I. D.; Jayanthi, R. K. R.; Al-Behadili, A. A.; Hassain, Z. A. A.; Ali, S. M.; Pau, G.; Livreri, P.; Aïssa, S. Design of a Planar Sensor Based on Split-Ring Resonators for Non-Invasive Permittivity Measurement. *Sensors* **2023**, *23* (11), 5306. https://doi.org/10.3390/s23115306.

(42) Javed, A.; Arif, A.; Zubair, M.; Mehmood, M. Q.; Riaz, K. A Low-Cost Multiple Complementary Split-Ring Resonator-Based Microwave Sensor for Contactless Dielectric Characterization of Liquids. *IEEE Sens. J.* **2020**, *20* (19), 11326–11334. https://doi.org/10.1109/JSEN.2020.2998004.

(43) Haq, T.; Ruan, C.; Ullah, S.; Fahad, A. K. Dual Notch Microwave Sensors Based on Complementary Metamaterial Resonators. *IEEE Access* **2019**, *7*, 153489–153498. https://doi.org/10.1109/ACCESS.2019.2948868.

(44) Lee, C.-S.; Bai, B.; Song, Q.-R.; Wang, Z.-Q.; Li, G.-F. Open Complementary Split-Ring Resonator Sensor for Dropping-Based Liquid Dielectric Characterization. *IEEE Sens. J.* **2019**, *19* (24), 11880–11890. https://doi.org/10.1109/JSEN.2019.2938184.

(45) Tsilipakos, O.; Maiolo, L.; Maita, F.; Beccherelli, R.; Kafesaki, M.; Kriezis, E. E.; Yioultsis, T. V; Zografopoulos, D. C. Experimental Demonstration of Ultrathin Broken-Symmetry Metasurfaces with Controllably Sharp Resonant Response. *Appl. Phys. Lett.* **2021**, *119* (23), 231601. https://doi.org/10.1063/5.0073803.

(46) Islam, M. R.; Islam, M. T.; M., M. S.; Bais, B.; Almalki, S. H. A.; Alsaif, H.; Islam, M. S.

Metamaterial Sensor Based on Rectangular Enclosed Adjacent Triple Circle Split Ring Resonator with Good Quality Factor for Microwave Sensing Application. *Sci. Rep.* **2022**, *12* (1), 6792. https://doi.org/10.1038/s41598-022-10729-4.

(47) Mehmet Bakır; Muharrem Karaaslan; Faruk Karadag; Sekip Dalgac; Emin Ünal; Oğuzhan Akgöl. Metamaterial Sensor for Transformer Oil, and Microfluidics. *Appl. Comput. Electromagn. Soc. J.* **2019**, *34* (05 SE-Articles), 799–806.

(48) Abdulkarim, Y. I.; Deng, L.; Karaaslan, M.; Altıntaş, O.; Awl, H. N.; Muhammadsharif, F. F.; Liao, C.; Unal, E.; Luo, H. Novel Metamaterials-Based Hypersensitized Liquid Sensor Integrating Omega-Shaped Resonator with Microstrip Transmission Line. *Sensors* **2020**, *20* (3), 943. https://doi.org/10.3390/s20030943.

(49) Islam, M. R.; Islam, M. T.; Hoque, A.; Soliman, M. S.; Bais, B.; Sahar, N. M.; Almalki, S. H. A. Tri Circle Split Ring Resonator Shaped Metamaterial With Mathematical Modeling for Oil Concentration Sensing. *IEEE Access* **2021**, *9*, 161087–161102. https://doi.org/10.1109/ACCESS.2021.3131905.

(50) Ivanov, A.; Agliullin, T.; Laneve, D.; Portosi, V.; Vorobev, A.; Nigmatullin, R. R.;

Nasybullin, A.; Morozov, O.; Prudenzano, F.; D'Orazio, A.; Grande, M. Design and Characterization of a Microwave Planar Sensor for Dielectric Assessment of Vegetable Oils. *Electronics* **2019**, *8* (9), 1030. https://doi.org/10.3390/electronics8091030.

(51) Canal Marques, A.; Cabrera, J.-M.; de Fraga Malfatti, C. Printed Circuit Boards: A Review on the Perspective of Sustainability. *J. Environ. Manage.* **2013**, *131*, 298–306. https://doi.org/https://doi.org/10.1016/j.jenvman.2013.10.003.

(52) Archambeault, B.; Brench, C.; Connor, S. Review of Printed-Circuit-Board Level EMI/EMC Issues and Tools. *IEEE Trans. Electromagn. Compat.* **2010**, *52* (2), 455–461. https://doi.org/10.1109/TEMC.2010.2044182.

(53) Grout, I. CHAPTER 3 - PCB Design; Grout, I. B. T.-D. S. D. with Fpga. and Cpld., Ed.; Newnes: Burlington, 2008; pp 123–176. https://doi.org/https://doi.org/10.1016/B978-0-7506-8397-5.00003-9.

(54) Chtioui, I.; Bossuyt, F.; Kok, M. de; Vanfleteren, J.; Bedoui, M. H. Arbitrarily Shaped Rigid and Smart Objects Using Stretchable Interconnections. *IEEE Trans. Components, Packag. Manuf. Technol.* **2016**, *6* (4), 533–544. https://doi.org/10.1109/TCPMT.2015.2511077.

(55) Tasolamprou, A. C.; Mentzaki, D.; Viskadourakis, Z.; Economou, E. N.; Kafesaki, M.; Kenanakis, G. Flexible 3D Printed Conductive Metamaterial Units for Electromagnetic Applications in Microwaves. *Mater. (Basel, Switzerland)* **2020**, *13* (17), 3879. https://doi.org/10.3390/ma13173879.

(56) Viskadourakis, Z.; Fanourakis, G.; Tamiolakis, E.; Theodosi, A.; Katsara, K.; Vrithias, N. R.; Tsilipakos, O.; Kenanakis, G. Fabrication of Mm-Scale Complementary Split Ring Resonators, for Potential Application as Water Pollution Sensors. *Materials (Basel).* **2023**, *16* (15), 5290. https://doi.org/10.3390/ma16155290.

(57) Nordin, A. N.; Abd Manaf, A. Chapter 2 - Design and Fabrication Technologies for Microfluidic Sensors; Mak, W. C., Pui Ho, A. H. B. T.-M. B., Eds.; Academic Press, 2023; pp 41–85. https://doi.org/https://doi.org/10.1016/B978-0-12-823846-2.00004-3.

(58) Yao, H.; Qiu, S.; Lv, Y.; Wei, S.; Li, A.; Long, Z.; Wu, W.; Shen, X. Indoor Particulate Matter Transfer in CNC Machining Workshop and The Influence of Ventilation Strategies—A Case Study. *Sustainability* **2023**, *15* (7). https://doi.org/10.3390/su15076227.

(59) Kumar, S.; Nassehi, A.; Newman, S. T.; Allen, R. D.; Tiwari, M. K. Process Control in

CNC Manufacturing for Discrete Components: A STEP-NC Compliant Framework. *Robot. Comput. Integr. Manuf.* **2007**, *23* (6), 667–676. https://doi.org/https://doi.org/10.1016/j.rcim.2007.02.015.

(60) Viskadourakis, Z.; Grammatikakis, K.; Katsara, K.; Drymiskianaki, A.; Kenanakis, G. Fabrication of Metasurfaces on Building Construction Materials for Potential Electromagnetic Applications in the Microwave Band. *Materials (Basel).* **2022**, *15* (20), 7315. https://doi.org/10.3390/ma15207315.

(61) Viskadourakis, Z.; Perrakis, G.; Symeou, E.; Giapintzakis, J.; Kenanakis, G. Transport Properties of 3D Printed Polymer Nanocomposites for Potential Thermoelectric Applications. *Appl. Phys. A* **2019**, *125* (3), 159. https://doi.org/10.1007/s00339-019-2469-0.

(62) Poiana, M.-A.; Alexa, E.; Munteanu, M.-F.; Gligor, R.; Moigradean, D.; Mateescu, C. Use of ATR-FTIR Spectroscopy to Detect the Changes in Extra Virgin Olive Oil by Adulteration with Soybean Oil and High Temperature Heat Treatment. **2015**, *13* (1), 689. https://doi.org/doi:10.1515/chem-2015-0110.

(63) Rohman, A.; Che Man, Y. B. Quantification and Classification of Corn and Sunflower Oils as Adulterants in Olive Oil Using Chemometrics and FTIR Spectra. *Sci. World J.* **2012**, *2012*, 250795. https://doi.org/10.1100/2012/250795.

(64) Moe Htet, T. T.; Cruz, J.; Khongkaew, P.; Suwanvecho, C.; Suntornsuk, L.; Nuchtavorn, N.; Limwikrant, W.; Phechkrajang, C. PLS-Regression-Model-Assisted Raman Spectroscopy for Vegetable Oil Classification and Non-Destructive Analysis of Alpha-Tocopherol Contents of Vegetable Oils. *J. Food Compos. Anal.* **2021**, *103*, 104119. https://doi.org/https://doi.org/10.1016/j.jfca.2021.104119.

(65) Barros, I. H. A. S.; Santos, L. P.; Filgueiras, P. R.; Romão, W. Design Experiments to Detect and Quantify Soybean Oil in Extra Virgin Olive Oil Using Portable Raman Spectroscopy. *Vib. Spectrosc.* **2021**, *116*, 103294. https://doi.org/https://doi.org/10.1016/j.vibspec.2021.103294.

(66) Viskadourakis, Z.; Sevastaki, M.; Kenanakis, G. 3D Structured Nanocomposites by FDM Process: A Novel Approach for Large-Scale Photocatalytic Applications. *Appl. Phys. A Mater. Sci. Process.* **2018**, *124*, 585. https://doi.org/10.1007/s00339-018-2014-6.

(67) Didham, M.; Truong, V. K.; Chapman, J.; Cozzolino, D. Sensing the Addition of Vegetable Oils to Olive Oil: The Ability of UV–VIS and MIR Spectroscopy Coupled with Chemometric Analysis. *Food Anal. Methods* **2020**, *13* (3), 601–607. https://doi.org/10.1007/s12161-019-01680-8.

(68) Borello, E.; Domenici, V. Determination of Pigments in Virgin and Extra-Virgin Olive Oils: A Comparison between Two Near UV-Vis Spectroscopic Techniques. *Foods* **2019**, *8* (1), 18. https://doi.org/10.3390/foods8010018.

(69) Miller, J. M. L.; Ansari, A.; Heinz, D. B.; Chen, Y.; Flader, I. B.; Shin, D. D.; Villanueva, L. G.; Kenny, T. W. Effective Quality Factor Tuning Mechanisms in Micromechanical Resonators. *Appl. Phys. Rev.* **2018**, *5* (4), 41307. https://doi.org/10.1063/1.5027850.

(70) Petersan, P. J.; Anlage, S. M. Measurement of Resonant Frequency and Quality Factor of Microwave Resonators: Comparison of Methods. *J. Appl. Phys.* **1998**, *84* (6), 3392–3402. https://doi.org/10.1063/1.368498.

(71) Zhong, Y.; Du, L.; Liu, Q.; Zhu, L.; Zou, Y.; Zhang, B. All-Silicon Terahertz Metasurface With Sharp Fano Resonance and Its Sensing Applications. *IEEE Photonics J.* **2021**, *13* (2),

1–10. https://doi.org/10.1109/JPHOT.2021.3065096.

(72) Jing, Z.; Jiaxian, W.; Lizhen, G.; Weibin, Q. High-Sensitivity Sensing in All-Dielectric Metasurface Driven by Quasi-Bound States in the Continuum. *Nanomaterials* **2023**, *13* (3), 505. https://doi.org/10.3390/nano13030505.

(73) Cong, L.; Tan, S.; Yahiaoui, R.; Yan, F.; Zhang, W.; Singh, R. Experimental Demonstration of Ultrasensitive Sensing with Terahertz Metamaterial Absorbers: A Comparison with the Metasurfaces. *Appl. Phys. Lett.* **2015**, *106* (3), 31107. https://doi.org/10.1063/1.4906109.